Cura, M. Erkin; Trebala, Michal; Ge, Yanling; Klimczyk, Piotr; Hannula, Simo-Pekka

Mechanical and tribological properties of $WO_{2.9}$ and ZrO_2 + $WO_{2.9}$ composites studied by nanoindentation and reciprocating wear tests

Published in:
Wear

DOI:
10.1016/j.wear.2021.203920

Published: 15/08/2021

Document Version
Publisher's PDF, also known as Version of record

Wear 478–479 (2021) 203920

Contents lists available at ScienceDirect

Wear

journal homepage: www.elsevier.com/locate/wear

Mechanical and tribological properties of $WO_{2.9}$ and ZrO_2 + $WO_{2.9}$ composites studied by nanoindentation and reciprocating wear tests

M. Erkin Cura [a,*,1], Michal Trebala [a], Yanling Ge [a,2], Piotr Klimczyk [b], Simo-Pekka Hannula [a]

[a] Department of Chemistry and Materials Science, Aalto University, P.O. Box 16100, FI-00076, Aalto, Finland
[b] Center of Advanced Manufacturing Technology, Lukasiewicz Research Network - Krakow Technology Institute, ul. Zakopianska 73, 30-418, Krakow, Poland

ARTICLE INFO

Keywords:
Crystallographic shear
Nanoindentation
Raman
Solid lubrication

ABSTRACT

Oxygen vacancies in $WO_{2.9}$ yield to formation of easy shear planes and they can potentially be applied in boundary lubrication conditions for reducing friction. Mechanical and tribological properties of pulsed electric current sintered monolithic $WO_{2.9}$ were studied by nanoindentation and nanoscratch, and the composites of ZrO_2 + $WO_{2.9}$ with reciprocating wear tests. Hardness of $WO_{2.9}$ at 25 °C was ~11 GPa and reduced elastic modulus was ~150 GPa. The ploughing dominated coefficient of friction as between 0.09 and 0.24 when measured against a Berkovich diamond tip. The composite n-ZrO_2 + 10 vol% $WO_{2.9}$ presented the lowest CoF, and wear rate 10^{-10} mm^3/Nm measured under 10 N load against alumina ball (6 mm diameter) due to $WO_{2.9}$ acting as a solid lubricant.

1. Introduction

The most common counter measure against wear and reducing friction in dry friction conditions is protecting surfaces of moving parts by hard coatings. Typically, nitrides and carbides of transition metals or carbon derivatives are applied as protective layers by different deposition techniques [1]. In recent years more studies focusing on friction properties of 2-D structures have been published [2] with emphasis on graphene lubrication [3] and carbon superlubricity [4]. Despite having superior mechanical properties, their common weakness is low oxidation resistance. Oxidation occurs by elevated ambient temperature [5] or because of heat generation by friction on material surface [6]. In either case, reducing friction of contacts by self-lubrication without surface modification can be beneficial. This is even more distinct under boundary lubrication conditions where surfaces are in contact at asperity couples and wear and friction are determined by the interaction between the solid bodies that are in contact [7]. This interaction typically yields heat generation due to friction and is detrimental on the wear mechanism [6]. In presence of a metal constituent, the increase in surface temperature leads to the formation of an oxide layer. This may either reduce the coefficient of friction (CoF), or increase it due to phase transformations and reactions occurring at counter materials' surfaces [6]. Under static or dynamic loading conditions the surface oxide may also deteriorate the mechanical properties of the material quickly.

Alternatively, it is possible to prevent surface oxidation and control the overall oxide content by introducing metal oxide supplements, i.e., oxide solid lubricants. Solid lubricants consist of different class of materials as the application areas may differ widely [8]. When applications for elevated temperatures are considered, preserving the lubrication properties and covering a wide range of operation temperatures emerge as two very important aspects discussed in depth in different reviews [9–11]. The most limiting factor regarding the aspects above is typically oxidation. This has been addressed e.g. by exploiting multiple constituents with synergistic effect [12] and designing adaptive structures combining metal oxides and oxide forming soft metals along with a hard matrix [13,14].

The shear properties and the amount of the formed oxide have considerable influence for self-lubrication. Ionic potential of the oxide in some cases can predetermine its friction properties when the metal oxide with higher ionic potential has its cations concealed by the surrounding anions, therefore their ability to interact and form strong bonding with other cations is restrained [15]. They can form covalent or ionic bonds that suppress their ability to shear when their ionic potential is lower. However, when the application temperature is above their melting

* Corresponding author. Aalto University, Department of Chemistry and Materials Science, Kemistintie 1, 02150, Espoo, Finland.
E-mail address: erkin.cura@aalto.fi (M.E. Cura).
[1] Current address: Murata Electronics Oy, Myllynkivenkuja 6, FI-01621 Vantaa, Finland.
[2] Current address: VTT Technical Research Centre of Finland Ltd., Kemistintie 3, 02150 Espoo, Finland.

https://doi.org/10.1016/j.wear.2021.203920
Received 9 September 2020; Received in revised form 12 March 2021; Accepted 9 April 2021
Available online 21 April 2021

Table 1
Summary of material compositions, sintering parameters, relative densities of the compacts, and adopted test methods.

Matrix	Additive	Sintering temperature, time and pressure	Relative density	Test methods
$WO_{2.9}$	–	1200 °C, 3 min, 75 MPa	~100%	Nanoindentation, Raman, XRD, SEM
n-ZrO_2	5 vol% n-WO_3[a]	950 °C, 5 min, 200 MPa	88.6%	Ball-on-disk, Raman, XRD, SEM
n-ZrO_2	5 vol% n-WO_3[a]	950 °C, 15 min, 200 MPa	90.7%	Ball-on-disk, Raman, XRD, SEM
n-ZrO_2	10 vol% n-WO_3[a]	975 °C, 10 min, 200 MPa	99.0%	Ball-on-disk, Raman, XRD, SEM
n-ZrO_2	20 vol% n-WO_3[a]	1000 °C, 10min, 200 MPa	99.0%	Ball-on-disk, Raman, XRD, SEM
t-ZrO_2	10 vol% n-WO_3[a]	950 °C, 15 min, 200 MPa	91.4%	Ball-on-disk, Raman, XRD, SEM
3YSZ	10 vol% n-WO_3[a]	950 °C, 15 min, 200 MPa	91.7%	Ball-on-disk, Raman, XRD, SEM

[a] WO_3 was fully transformed into $WO_{2.9}$ during sintering.

point, low melting point oxides that are applied as solid lubricants can reduce friction significantly, and there are few oxides with identical ionic potentials that can have highly different friction properties [16]. Some oxides on the other hand, possess "easy shear planes". They have relatively low shear strength in certain lattice orientations in their crystal structure due to missing plane of oxygen atoms called a crystallographic shear (CS) plane [17].

Metal oxides with CS planes in their lattice have a potential for reducing friction owing to their lattice structure. These oxides are called Magnéli phase oxides after A. Magnéli who first observed the oxygen deficient phases in Mo–O system [18,19], and then reported the homologues series of oxygen deficient metal oxides in Mo–O and W–O systems [20]. Studies in Ti–O and V–O systems were followed by others [21,22]. It was Gardos [23] who first exploited the effect of anion deficiency on tribological application of TiO_{2-x} and investigated tribological behaviour of $TiO_{1.7-2}$ between 25 °C and 1000 °C. He reported a decrease in shear strength from 21 MPa to 8 MPa yielding a CoF of ~0.08 against sapphire when there is a small deviation from TiO_2 stoichiometry to $TiO_{1.98}$ [24]. He further addressed the formation of CS oxides on the sliding surfaces, to motion, heating and varying oxygen amount during wear tests [25,26]. Woydt and his co-workers [27] reported reduced wear by tribologically induced Ti_nO_{2n-1} in TiN and TiN composites with SiC and Si_3N_4 during dry sliding at elevated temperatures. When they hot pressed pure Ti_4O_7 or Ti_4O_7/Ti_5O_9 the CoF was as low as 0.2 at 23–400 °C, and 0.4 at 800 °C [28]. They also achieved higher wear resistance, when Ti_4O_7/Ti_5O_9 was thermally sprayed [29]. Comprehensive work of Woydt on sub-stoichiometric oxides with emphasis on technological applications can be found in Ref. [30].

Formation of lubricious oxides in V–O system during high temperature wear was studied by Gassner et al. [31], Fateh et al. [32] and Franz and Mitterer [33]. Sputtered V_2O_5 films have lower CoF below the melting point than when it is exceeded. This behaviour indicates that easy shear V_nO_{2n-1} structures are more efficient for lubrication than melting of the oxide phases at elevated temperatures.

Less studies are made on Mo and W lubricious oxides focusing mainly on by-products of oxidation of MoN or WN phases. Based on their observations Gassner et al. [34] attributed low friction in MoN and WN to the formation of various Mo_nO_{3n-1} and W_nO_{3n-1} phases, although they were observed in thermal stability tests of their stoichiometric oxides but not on contact surfaces during friction. In a previous study we reported the presence of Mo_4O_{11} and MoO_3 in wear tracks of Al_2O_3 + Mo composites tested at 400 °C under dry sliding conditions against alumina [35]. Even though W–O system exhibits more stable potentially lubricious oxide phases, only few studies have been made for their tribological benefits [36,37], and none for the systems that contain easy shear oxides of W_nO_{3n-1} or W_nO_{3n-2}.

Pulsed electric current sintering (PECS) is a powerful method for consolidation of wide variety of materials from low melting point metals to ultra-high temperature ceramics. It is a pressure assisted and current activated sintering method, with shortcomings of uniaxial pressing. During PECS, densification occurs not only by mass transport phenomena but also with the help of electron flow and thereby electroplasticity. Electron flow promotes mobility of dislocations by increasing the energy around lattice defects, which ultimately enhances the atomic vibrations in the area and reduces the flow stress of the material during sintering [38]. The ceramic composites were synthesized by PECS benefiting from its rapid densification, while exploiting its reducing effect.

The present study focuses first on the mechanical and friction properties of oxygen deficient tungsten oxide phase $W_{20}O_{58}$ ($WO_{2.9}$) and then seeks answer to the question if it is possible to utilize this phase in a ceramic matrix composite as a solid lubricant at room temperature.

2. Materials and methods

2.1. Powder preparation and consolidation

For the synthesis of $WO_{2.9}$ a simple method similar to that of A. Magnéli [18] was followed. The mixture of WO_3 (Sigma-Aldrich, > 99%, <20 μm) and W powders (Sigma-Aldrich, 99.95%, <1 μm) in the corresponding stoichiometric ratio (~37:1 in wt%) were homogenized in a Retsch Mixer Mill MM 400 placed in a glovebox, at 20 s^{-1} for 5 min in Ar atmosphere to obtain a well dispersed powder mixture. The powder mixture was sealed in a quartz tube in vacuum and annealed at 1220 °C for 360 h to yield $WO_{2.9}$. Prior to vacuum sealing, powders were pre-compacted applying 5 MPa pressure and flushed with Ar for eliminating the residual oxygen.

Composite powders were prepared mixing nano-sized ZrO_2 (n-ZrO_2, Sky Spring Nanomaterials, 99.9%, 20–30 nm) and nano-sized WO_3 (n-WO_3, Sky Spring Nanomaterials, 99.5%, <100 nm) in the amounts of 5, 10 or 20 vol%, in a planetary ball mill (Fritsch P6) in ethanol for 2 h. Micron-sized ZrO_2 (t-ZrO_2, Tosoh Co., >99.9, 600 nm, in 60 μm granules) and yttria stabilized ZrO_2 (3YSZ, Inframat Advanced Materials, > 99.9%, <500 nm) were also tested as matrix materials and mixed by the same method with 10 vol% n-WO_3. Although the study aims at acquiring ZrO_2 matrix composites that contain $WO_{2.9}$ as solid lubricant, WO_3 was used as starting powder, which was transformed into $WO_{2.9}$ during sintering.

For the consolidation of powders into dense compacts pulsed electric current sintering (PECS) was adopted. Sintering of monolithic $WO_{2.9}$ was conducted at 1200 °C in a vacuum of 8 Pa applying pressure of 75 MPa (HP D25/2 FCT System GmbH). The powder mixtures were compacted in graphite moulds with a graphite foil liner and the temperature control was maintained by a vertically located optical pyrometer reading the temperature through the upper punch from graphite surface 5 mm above the sample. The heating rate and the sintering dwell time was 100 °C/min and 3 min, respectively. The sintered compact diameter was 20 mm and thickness 5 mm.

Composite powder mixtures were consolidated by PECS at 950–1000 °C for 5–15 min. Heating rate of 75 °C/min was used for compactions and due to relatively low sintering temperatures, 200 MPa pressure was applied for improving the densification. The applied pressure and heating rate were kept the same for all materials. High pressure was only possible when WC–6Co lined with graphite foil were utilized instead of graphite moulds. The specimens in all compactions were 20 mm in diameter and 3 mm in height. Densities of the sintered compacts were determined by Archimedes' method. Sintering parameters, the relative densities of the compacts and applied test methods are summarised in Table 1.

Table 2
Parameters for angular reciprocating friction tests.

Parameter	Value
Linear speed	5 cm/s
Radius	5 mm
Angle	45°
Cycles	4000
Load	1 N, 5 N 10 N, 20 N
Frequency	4.05 Hz
Distance	32 m
Counter material	Al_2O_3, d: 6 mm
Humidity	50%
Temperature	23 °C

2.2. Characterisation of the phase and microstructure

Formation of intended phases following vacuum annealing and consolidation was studied by X-ray diffraction (XRD) applying Cu-K_α radiation with a step size of 0.002° (Pananalytical X'pert Pro MPD Powder). Raman spectroscopy (Horiba Jobin-Yvon, LabRAM HR UV-NIR) was adopted for identifying the CS oxide following vacuum annealing and verifying its structure after PECS. It was also utilized for studying the wear tracks. Wear tracks of the composites were also evaluated by scanning electron microscopy (SEM, Hitachi S4700).

2.3. Mechanical and tribological measurements

The hardness (H), reduced elastic modulus (E_r) and coefficient of friction of the sintered compacts were investigated by nanoindentation and scratch tests against diamond tips employing Hysitron TriboIndenter TI-950. Indentation tests at room temperature were conducted with a Berkovich tip ($\theta = 65.27°$, tip radius of 0.100 μm), applying the loads of 500 μN, 1000 μN, 5000 μN and 10000 μN. The tests were conducted under load control. The time for reaching the maximum load was 5 s, then followed by a hold of 2 s and unloading in 5 s. The CoF of the sintered compacts were studied with the same Berkovich tip as well as with a cono-spherical diamond tip (will be referred as spherical tip, $\alpha = 90°$, tip radius of 0.225 μm) applying the loads of 10 μN, 50 μN, 100 μN, 500 μN and 1000 μN. The scratch tests were performed by applying three single scratches with length of 10 μm on the material surface for each applied load to obtain CoF. The surface roughness (R_q) at the scratch area was obtained by scanning probe microscopy (SPM) that was made prior to the scratch tests with a Berkovich tip in the TI950.

Reciprocating ball-on-disk tests were adopted for studying the wear and friction behaviour of the compacted ceramic composite discs against alumina (Al_2O_3) balls having a diameter of 6 mm (Anton Paar). During the tests the disc samples were moving in reciprocal manner around their centre axis, and the counter ball was stationary. In an angular reciprocal movement, the angle was changed for achieving the same sliding distance at different locations on radius of test samples. Samples were tested two times for each applied normal load. The exceptions were sample n-ZrO_2 + 10 vol% $WO_{2.9}$ (950 °C, 10 min), which was measured three times when 10 N normal load was applied for verifying the relatively low results, and n-ZrO_2 + 10 vol% $WO_{2.9}$ at 20 N which was broken after the first test. The test parameters are summarised in Table 2. After the friction tests a stylus type profilometer (Veeco Dektak 6M) was applied to determine wear rates. In addition, wear tracks were analysed by optical microscopy, electron microscopy and Raman spectroscopy for the identification of tribo-products.

3. Results

3.1. Synthesis of $WO_{2.9}$ and its composites with ZrO_2

The oxygen deficient phase $WO_{2.9}$ was synthesized from milled WO_3 and W powder mixture applying vacuum annealing at 1220 °C for 360 h. Particles with columnar shape were acquired (Fig. 1). The columnar structures were up to several hundreds of microns in length and as wide as 8 μm. XRD showed that stoichiometric mixture of WO_3 and W was fully transformed into $WO_{2.9}$ (Fig. 2a). The peak positions in XRD

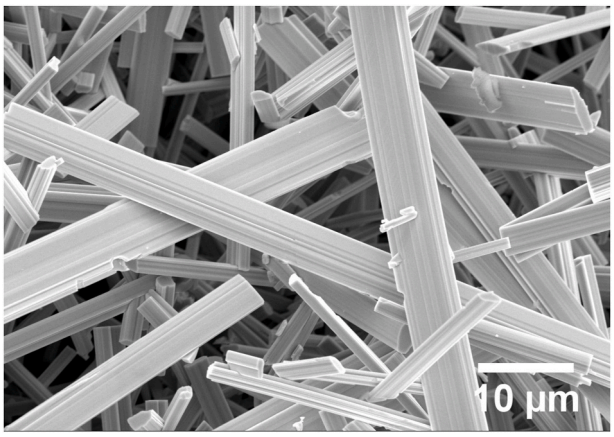

Fig. 1. SEM image of WO_{3-x} particles after vacuum annealing at 1220 °C.

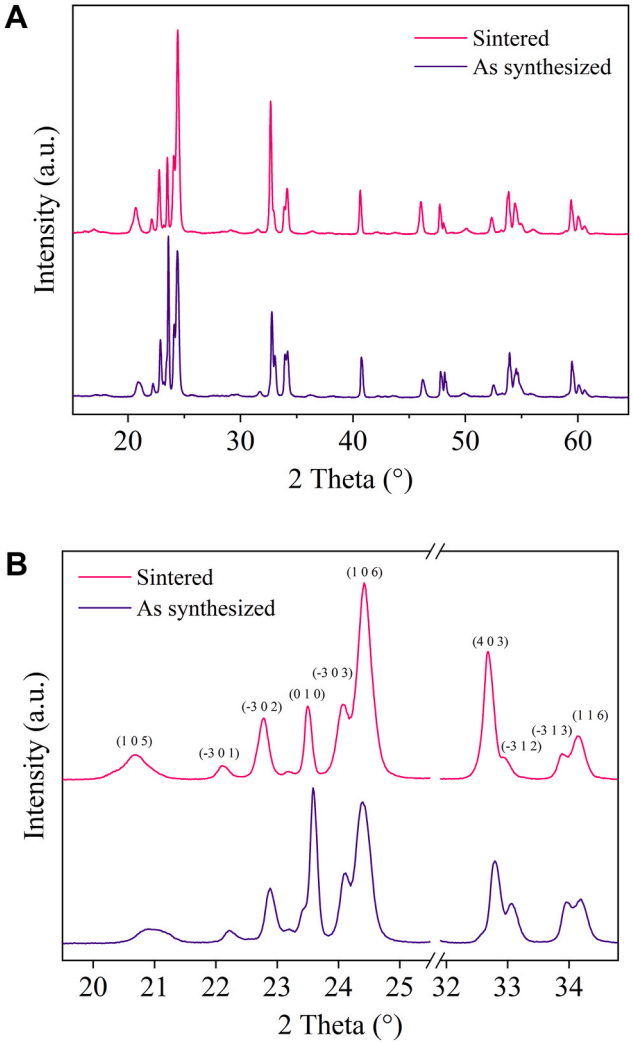

Fig. 2. (a) X-ray diffraction spectra of $WO_{2.9}$ in powder and bulk forms and (b) comparison of major peaks.

Table 3
Calculated lattice parameters of $WO_{2.9}$ (annealed at 1220 °C) before and after sintering.

Parameter	Powder	Sintered
a (Å)	12.0682	12.0850
b (Å)	3.7787	3.7826
c (Å)	23.6489	23.6505
alpha (°)	90	90
beta (°)	94.7113	94.6911
gamma (°)	90	90
Crystal system	Monoclinic	Monoclinic

spectra were similar to those of Booth et al. [39], with a few exceptions that are consistent with Magnéli's work [40]. The synthesized powder was milled to reduce fibres into smaller particles prior to XRD studies. Despite the milling, some preferred orientation was observed within the XRD spectra due to faceted morphology of the whiskers. Bulk cylinder-shaped samples with a density of 7.17 g cm^{-3} were obtained when the powder was consolidated. No phase changes occurred and both powder and sintered bulk were monoclinic phase with space group P2/m, but after sintering, $WO_{2.9}$ was found to have somewhat textured structure obviously due to uniaxial loading during sintering (Fig. 2b). The strong (010) peak was decayed and the (106) peak had the highest intensity and peak (403) also got stronger. The lattice parameters of $WO_{2.9}$ in sintered and powder forms were calculated (Table 3) according to PDF: 01-073-2182 from ICSD, based on the structure from Ref. [40]. Change in peak intensities were referred to combination of morphology of the particles and uniaxial pressing during sintering. Minor shift in peaks positions was also observed probably due to distortion in atomic positions of oxygen atoms and stress that was introduced during sintering.

Following the synthesis of $WO_{2.9}$ powder, ceramic composites were prepared initially by introducing $WO_{2.9}$ into n-ZrO_2. Two major challenges in synthesis of bulk composites were, *(i)* phase transformation of WO_{3-x} due to its complex stoichiometry (Fig. 3a) [41], and *(ii)* avoiding reactions between ZrO_2 and WO_{3-x} (Fig. 3b) [42]. Although sintering of the composite powders was successful, $WO_{2.9}$ was transformed into $WO_{2.72}$, and when sintering temperature was approximately 1100 °C ternary compounds were formed in Zr–O–W system (Fig. 3b). While $WO_{2.9}$ ($W_{20}O_{58}$) belongs to W_nO_{3n-2} homologous series, $WO_{2.72}$ ($W_{18}O_{49}$) does not and its structure was not preferred in this study. As focus was exploiting the CS structure in W–O system, ternary phases were not desirable either (Fig. 3b). For solving the first issue, the reducing ambient of PECS furnace was put into use [43]. In order to obtain the desired stoichiometry n-WO_3 powders were mixed with n-ZrO_2 matrix as reinforcement additive instead of $WO_{2.9}$. Standard graphite tools in PECS react with residual oxygen in the vacuum chamber as well as the oxide sample, hence formation of CO creates a highly reducing ambience. Reducing effect in PECS process is a known

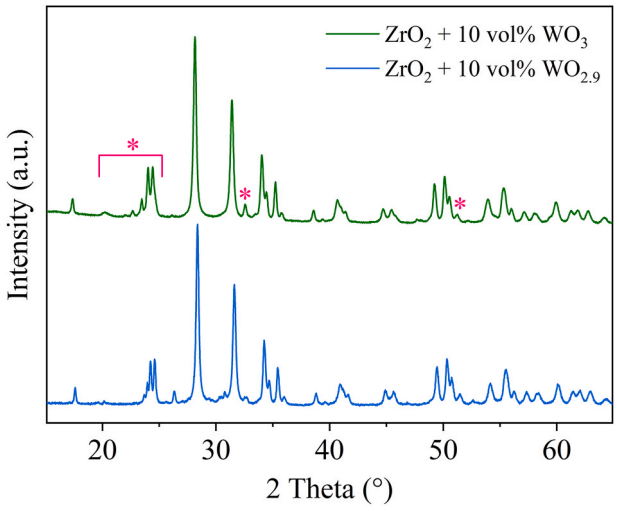

Fig. 4. Comparison of XRD spectra of sintered composites from starting powders of ZrO_2 + 10 vol% $WO_{2.9}$ and ZrO_2 + 10 vol% WO_3. Marked peaks refer to the most characteristic peaks of $WO_{2.9}$.

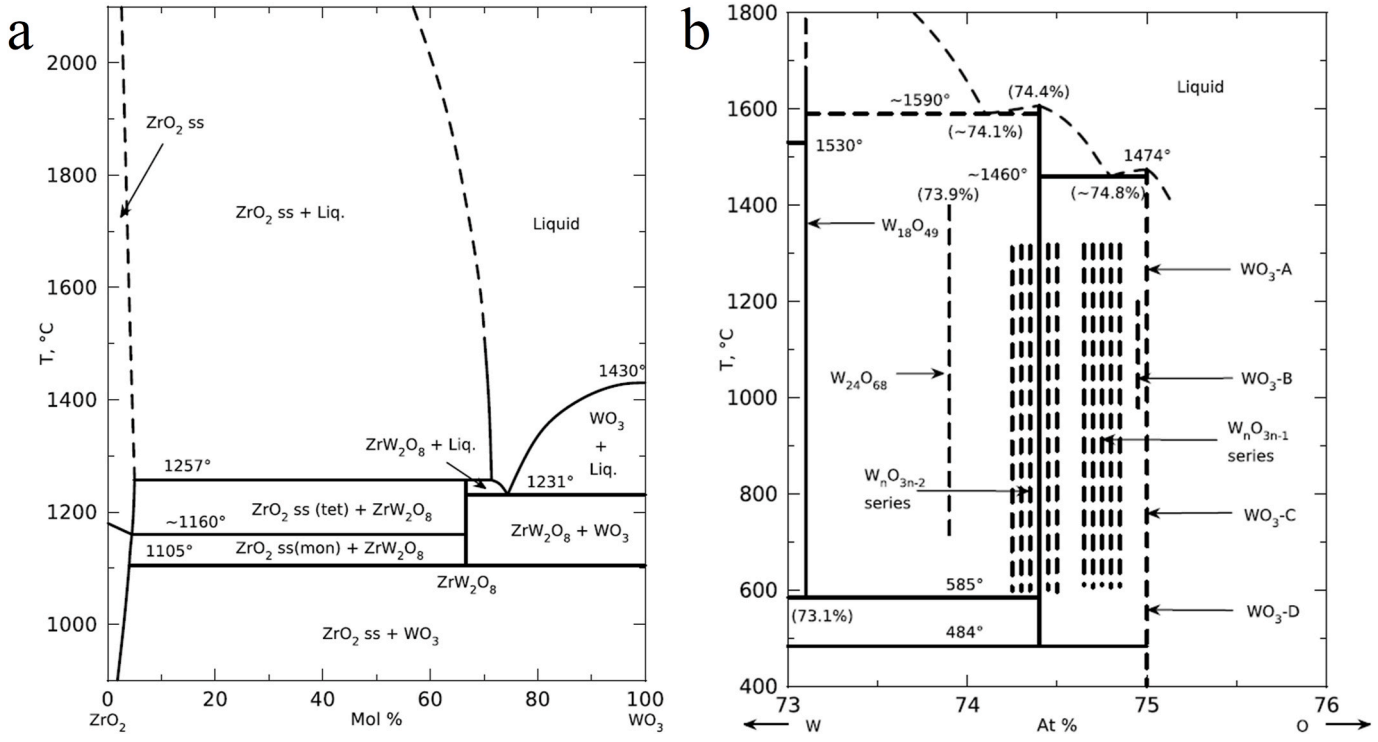

Fig. 3. Phase diagrams of (a) W–O with lower oxides, and (b) ZrO_2–WO_3 (reproduced from Refs. [41,42], respectively).

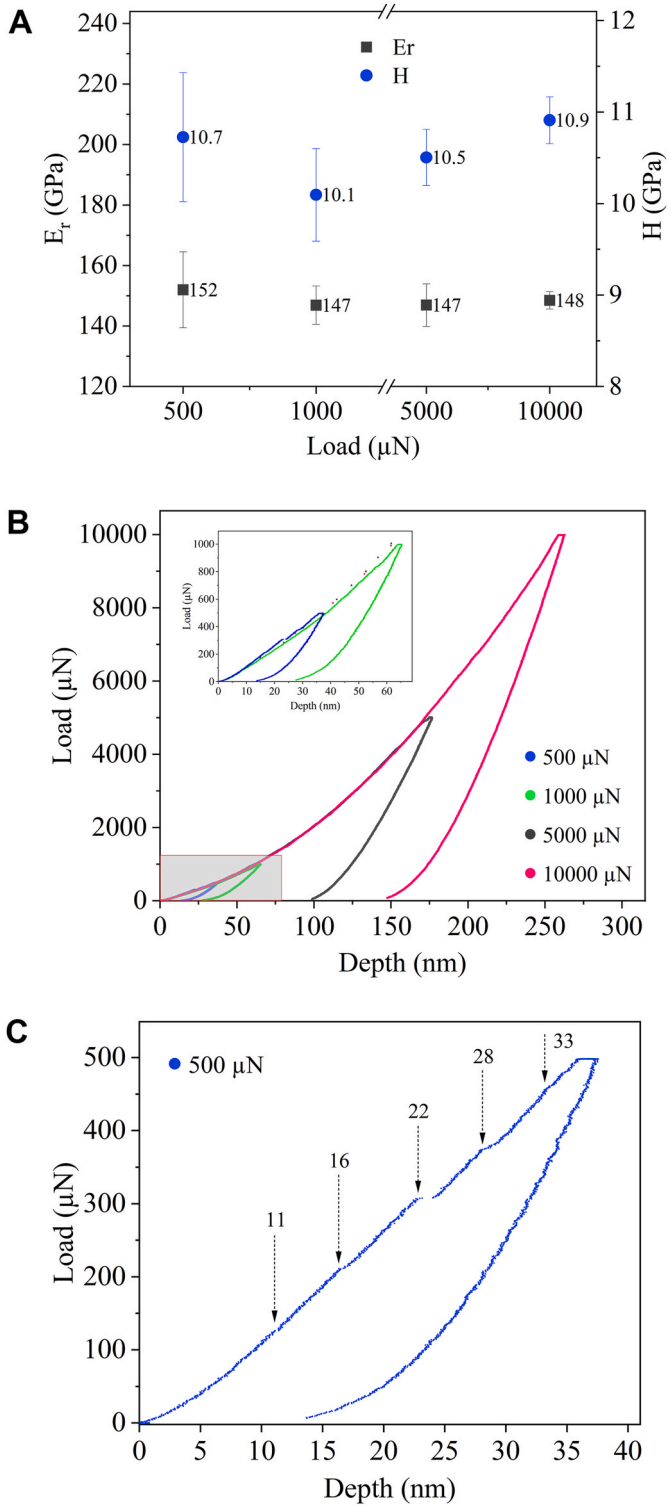

Fig. 5. (a) Reduced modulus and hardness of $WO_{2.9}$ as a function of load. (b) Force/displacement curves from nanoindentation, with curves of 500 μN and 1000 μN tests in-picture. c) Pop-in effect in 500 μN curve with corresponding depth values marked.

phenomenon. Typically, sintered oxides end up having dark grey regions on their surface [44]. The coloration has been widely investigated for transparent oxides [45], which was attributed to emerging point defects in oxides owing to reducing environment in PECS. We observed similar results in our earlier work (unpublished data) with alumina that was translucent with dark grey zones on its surface, and with YSZ emitting red colour when exposed to X-rays (also published by others [46]), both due to oxygen vacancies. In Fig. 4, the marked peaks in XRD spectra of sintered ZrO_2 + WO_3 refer to the most characteristic peaks of $WO_{2.9}$ confirming the transformation of WO_3 into $WO_{2.9}$. The same peaks are missing from the spectra of sintered ZrO_2 + $WO_{2.9}$, owing to the transformation of $WO_{2.9}$ into lower oxides (e.g. $WO_{2.72}$). Monoclinic ZrO_2 peaks were in well correspondence with reference pattern PDF: 01-083-0944 from ICDD. To cope with the second challenge, the sintering temperature was kept at 950 °C, which was low for decent densification. Therefore, high-pressure moulds and sintering pressure of 200 MPa were utilized during PECS for improving densification.

3.2. *Mechanical and friction properties of $WO_{2.9}$*

Pure $WO_{2.9}$ presented a hardness of 10.1–10.9 GPa and an elastic modulus (E_r) of 147–152 GPa obtained by nanoindentation performed with a Berkovich tip. The change in hardness is well below 10%, and considering the standard deviation limits of the measurement system (e.g. accuracy of calibration for fused silica being ±10% for H and ±5% for E_r) the values obtained for H and E_r do not thus meaningfully vary with the load (and the depth). According to previous measurements [47] on stoichiometric tungsten (VI) oxide (WO_3) sputtered thin films, hardness of 13.74 ± 0.2 GPa in amorphous form and 15 ± 0.5 GPa when crystalline and measured at 30 nm penetration depth by nanoindentation was obtained. Correspondingly, Young's modulus values of 164 ± 5 GPa and 193 ± 1 GPa for amorphous and crystalline films, were obtained with the same technique at room temperature. It is therefore reasonable to assume that the oxygen deficiency, and emerging easy shear planes thereof in our measurements have reduced the hardness of $WO_{2.9}$ in comparison to that of WO_3. During indentation small plastic deformation activated pop-in events [48] were observed as manifested in the load-depth curves in Fig. 5b and c. As the loading time for different maximum loads was constant, the loading rate increased with increasing maximum load making observation of pop-in effects difficult at higher loads [49]. At each maximum load during the hold a short period of stress relaxation can be observed, when the tip penetrates further into the sample. This is an evidence of viscoplasticity in the specimen [59]. The indentation marks observed by SPM are shown in Fig. 6. SPM can detect clear marks only from indentations with 5000 μN and 10000 μN.

Friction properties of pure $WO_{2.9}$ were studied applying Berkovich and spherical diamond tips as a function of applied load (Fig. 7). In nano friction tests, $WO_{2.9}$ showed low CoF when tested against Berkovich tip. Initially the CoF was very low under 10 μN load, and it reached almost a plateau between 0.19 and 0.24 when the normal load was increased further. Against Berkovich geometry the CoF remained steady during the early part of the scratch and the CoF was calculated from the first half of the scratch. CoF was approximately 0.1 (0.09 ± 0.067) under 10 μN load, and approximately 0.2 for other loads (0.22 ± 0.019, 0.19 ± 0.009, 0.23 ± 0.007 and 0.24 ± 0.005 for 50 μN, 100 μN, 500 μN and 1000 μN load, respectively). When the applied load was 10 μN, higher scatter was observed due to signal noise from the measurement system. Fig. 8 shows the images of the scratches from three scratch tests and their corresponding profiles, for two tip geometries. The scratch lines are clearly visible in post-indentation SPM images after the scratch under 1000 μN (Fig. 8a and b). The penetration depth at the highest normal load was consistent with nanoindentation results and was approximately 60 nm according to the force curves, which indicates the interaction between the tip and the test surface was at both pyramidal and rounded sections of the Berkovich tip. The maximum height for pile-up was approximately 15 nm according to line scan from SPM image (Fig. 8d).

When the same tests were made applying a spherical tip, the CoF was similar to those with the Berkovich tip, i.e., CoF was 0.17–0.18 up to 100 μN. At higher loads the CoF increased to 0.57 under 500 μN and eventually to 0.64 under 1000 μN. At the latter loads CoF was increased because of ploughing. The maximum penetration depth was about 250

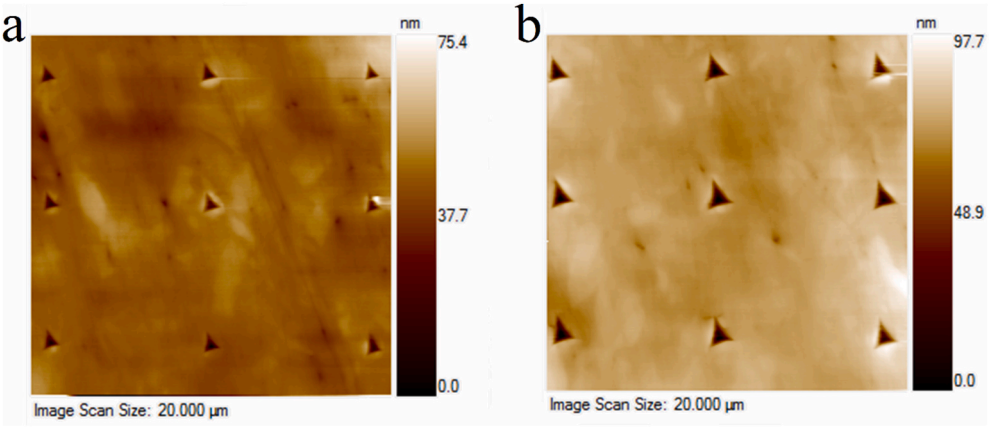

Fig. 6. SPM images of indent marks after indents with (a) 5000 µN and (b) 10000 µN.

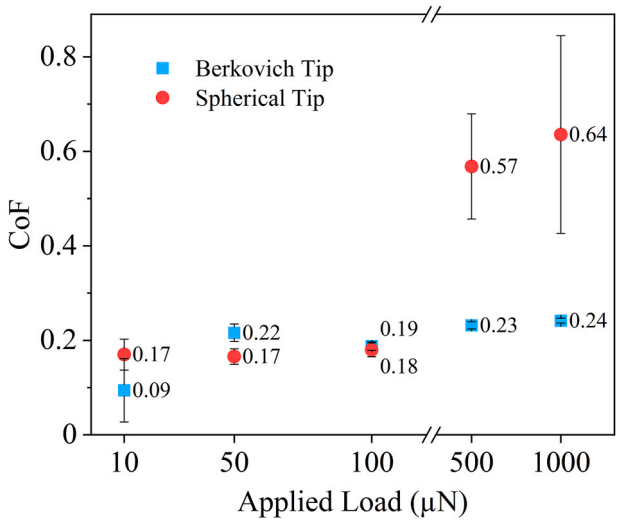

Fig. 7. Change in CoF of $WO_{2.9}$ under different loads with Berkovich and spherical tips.

nm based on the force curves and the highest pile-up was approximately 60 nm on the SPM image line scans (Fig. 8e). The pileups were much larger compared to Berkovich tip owing to differences in tip geometry. The width of the scratch marks at the highest load was approximately 0.42 µm and 0.25 µm for Berkovich and spherical tips, respectively. The cone angle for spherical tip was 90° and equivalent cone angle of Berkovich tip was approximately 140.6°. Therefore, spherical tip showed higher penetration. Accordingly, when moving under higher loads ploughing hindered sliding of the spherical tip, but Berkovich tip was not affected from ploughing as much owing to scratch direction being from bottom to top by sharp corner head-on (Fig. 8c). The surface R_q at the 20 µm × 20 µm area was 3.2 nm and 5.9 nm, at the sites where the scratches were performed with Berkovich and spherical tips, respectively.

3.3. Tribological properties of ZrO_2 + $WO_{2.9}$ composites

Friction properties of the composites were measured under different normal loads, against varying $WO_{2.9}$ amount and different matrix materials. The maximum amount of $WO_{2.9}$ was limited to 20 vol% for sustaining the mechanical strength of the composite, while forming a continuous tribolayer for reducing friction. In the present tests 1 N normal load was insufficient to activate low friction mode via CS planes. Lower CoF was obtained at 5 N and 10 N. Under 20 N, surface cracks were observed, yielding to higher CoF. The same trend was observed for all the material compositions. When all the test samples considered, the CoF was reduced by 31–42% when normal load was increased from 1 N to 5 N. The lowest CoF was observed when normal load was 10 N and the drop in CoF was 74–86% (compared to 1 N). When the test load was 20 N the CoF stayed almost unchanged (Fig. 9a). The lowest CoF result was 0.108 ± 0.030 for n-ZrO_2 + 10 vol% $WO_{2.9}$, which was sintered at 975 °C for 10 min, under 200 MPa pressure. In presence of 20 vol% $WO_{2.9}$ the friction properties were quite similar to composites with less additives, but the test sample was completely scattered after the test, despite good densification. The friction properties were better when the matrix material was n-ZrO_2 compared to t-ZrO_2 or 3YSZ (Fig. 9b). Different sintering durations were tested for checking any phase transformations during consolidation.

The composites experienced wear rates in the order of 10^{-10} mm^3/Nm, with a several fold difference. The n-ZrO_2 + 10 vol% $WO_{2.9}$ had the lowest wear rate of 4.82×10^{-11} mm^3/Nm under 10 N normal load. This was an order of magnitude lower than that of the other composites. Test materials showed the same trend in their wear behaviour as they did in their friction properties, therefore SEM images only for n-ZrO_2 + 10 vol % $WO_{2.9}$ are presented. The width of wear tracks under different loads showed considerable difference (Fig. 10).

During the interaction between alumina ball and composite surface, roughening of the surface was observed in all wear tracks. Although a tribolayer was visible in all tracks, the wear track was smoother in 5 N and 10 N scars. The grain structure of ZrO_2 was clearly visible in 5 N track, but not in 10 N track. The tribolayer was removed during sliding of alumina ball and when applied load was 10 N, the formed tribolayer covered the wear scar letting the counter material move easily on the flat (Fig. 11a and b). When the applied load was increased to 20 N tearing and spalling was observed within the wear track (Fig. 11c). Plastic deformation was dominant mechanism during ball-flat interaction as the load increased. The Hertz maximum contact pressures for n-ZrO_2 + 10 vol % $WO_{2.9}$ at the ball – flat contacts were 0.82 GPa, 1.40 GPa, 1.76 GPa and 2.22 GPa for 1 N, 5 N, 10 N and 20 N normal loads, respectively. The results were very similar for all the composites. When the normal load was 20 N, the contact pressure was too high causing alumina ball to sink into the surface and under 1 N the protective low friction mechanism was not activated (Fig. 11d).

Raman spectroscopy was implemented for identifying the oxide phases within wear tracks. Firstly, measurements were performed on $WO_{2.9}$ as the reference material in powder form after vacuum annealing and following sintering. The CS oxide phase remained unchanged after the sintering despite that the sub-oxide phases are prone to deviation from their stoichiometry relative easily (Fig. 12a). Chen et al.'s measurement results on $W_{20}O_{58}$ nanowires were adopted as reference in our measurements [50]. Similarly to Chen et al. for monoclinic [50] and

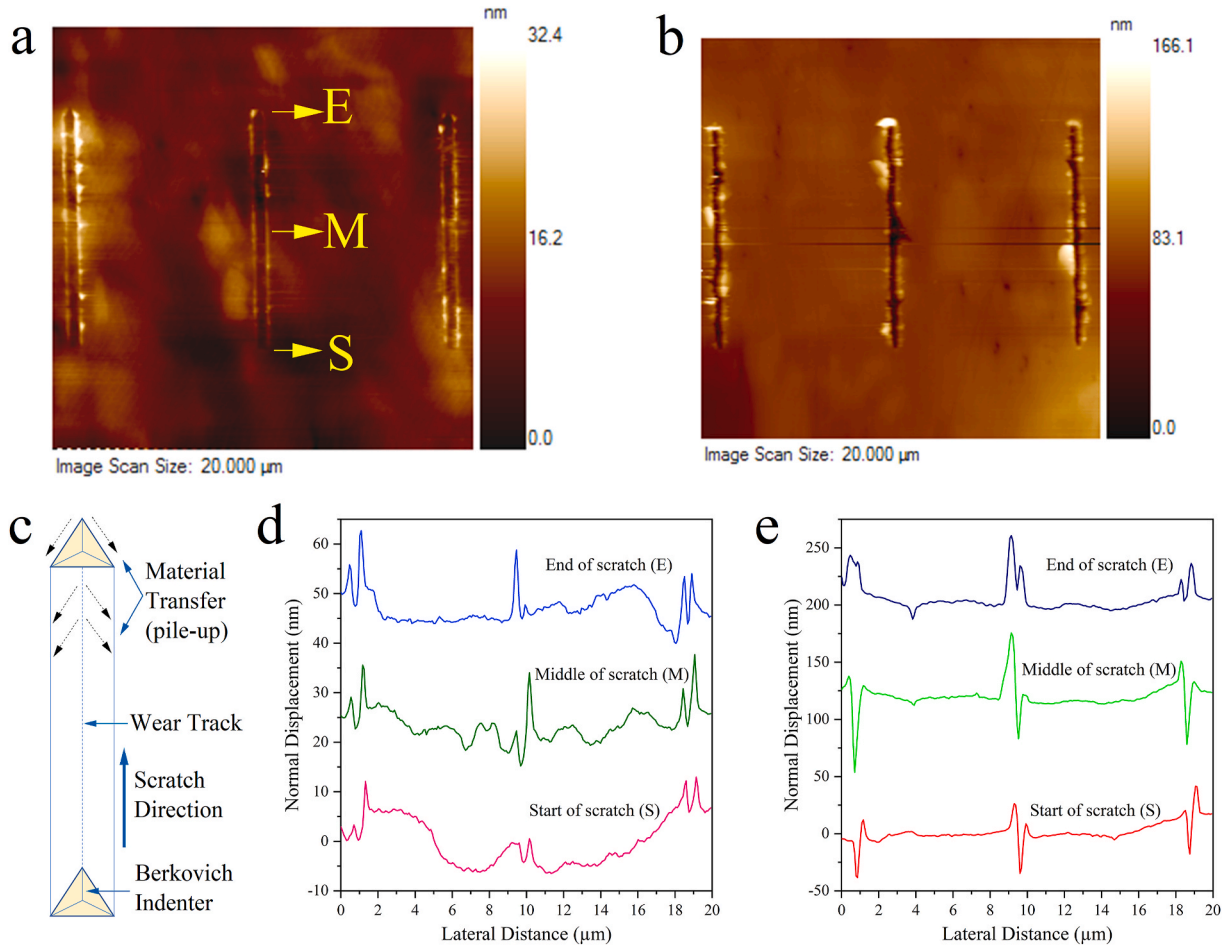

Fig. 8. SPM images after scratch tests by nanoindentation for (a) Berkovich and (b) spherical geometries using 1000 µN load. c) Scratch orientation for Berkovich tip. Line profiles of the scratch lines for d) Berkovich and e) spherical tips, from the start, middle and end of the scratch.

Frey et al. for tetragonal phases before [51], Raman spectrum of $WO_{2.9}$ had very strong background compared to that of WO_3 due to absorption. In addition, $WO_{2.9}$ and WO_3 have several major peaks in the same band region, both of which make identification of the peaks challenging. The Raman spectrum of $WO_{2.9}$ shows similarities with stoichiometric WO_3 in many ways, but also some clear distinctions (Fig. 12b). According to Frey at al. CS WO_{3-x} phases have several distinct W–O – W bond lengths, and there are quite many bands below 600 cm^{-1}. Their W–O – W bonds are shorter compared to WO_3 owing to edge sharing octahedra, shifting the modes above 800 cm^{-1} to higher energies [51]. There are a few differences with our work and the aforementioned references, namely the synthesis method of the oxide and the applied reductant. With the support of XRD measurements, CS oxide synthesis was concluded to yield complete transformation of WO_3 into $WO_{2.9}$ and was well correlated with XRD spectrum of $W_{20}O_{58}$ in PDF: 01-083-0944 from ICDD. Furthermore, Raman spectrum of $W_{20}O_{58}$ had several extra bands at around 65 cm^{-1}, 100 cm^{-1}, 965 cm^{-1}, and a strong band at around 815 cm^{-1} instead of the bands at 804 cm^{-1} and 830 cm^{-1}, with some shift in other bands (Fig. 12b). A more detailed discussion on this will follow in a later section. Analysis of the reference material was followed by analysis of the sintered composites (Fig. 12c). For clarity, results from the wear track having the lowest CoF are presented (Fig. 12d). The most noticeable difference was less pronounced background in the spectra, which resulted in better peak fitting. Dominant bands in our reference material below 400 cm^{-1} were also visible in the spectrum of composite material both from outside and inside the wear track. The spectrum from the wear track had the dominant band at 812 cm^{-1} with minor deviation from 815 cm^{-1} of the reference material and with the band emerging at 830 cm^{-1} (Fig. 12d). The band frequencies in Raman spectrum are referred to vibrations at certain bonds, and if a certain bond type is more exposed owing to strong anisotropy and preferred orientation, the related band will be prominent and vice versa. The reference material ($WO_{2.9}$) had well oriented crystals with elongated and faced columnar morphology, hence intensity and even exact location of the bands differ between different studies unless measurements are performed from the same plane orientation. When a wear track is considered, the formed tribolayer is made of several different randomly mixed materials. Despite the small area of analysis, the crystal orientation of constituting phases will be different at different spots. Therefore, it is possible to attribute the changes in peak intensities and minor shifts in their positions to local orientation.

4. Discussion

4.1. Materials synthesis and consolidation

Consolidation of the composites is important for obtaining the desired phase structure and mechanical and tribological properties of the CS oxide phase. Two main issues in consolidation of ZrO_2 + $WO_{2.9}$ composites were earlier described as preventing formation of ternary oxides and maintaining $WO_{2.9}$ stoichiometry. The first one was achieved with the help of reducing atmosphere in PECS process and the second one required reduction of sintering temperature considerably. In our tests we were not able to achieve the desired CS oxide phase in the sintered compacts when the additive in the starting composite powder was $WO_{2.9}$, i.e., some reduction occurred to lower oxides such as $WO_{2.72}$

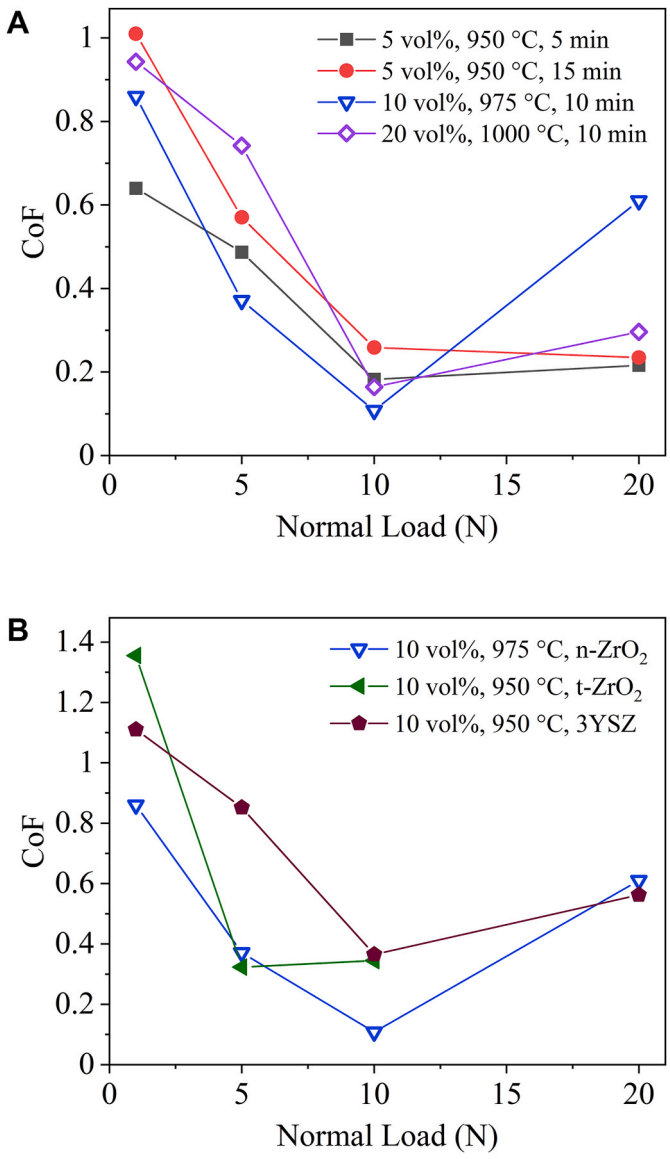

Fig. 9. Evolution of CoF versus applied load with different (a) $WO_{2.9}$ content and (b) starting material.

during sintering. However, when n-WO_3 was used as starting material, it was reduced during PECS process [43] giving the desired ZrO_2 + $WO_{2.9}$ composite. The starting powders ZrO_2 and WO_3 had white and very light-yellow colour, respectively, but the sintered compacts had a mixture of dark blue and white, which also implies reduction of WO_3 into WO_{3-x}. In our work, although WC–Co moulds were utilized for applying higher pressure, the adopted graphite foil onto the inner surface of the body part and between the powder and the punch surfaces, as well as graphite spacers between the electrodes and the moulds are expected to be responsible for generating the reducing environment. As a result, it was possible to reduce WO_3 of the starting powder to $WO_{2.9}$ during sintering. Although sintered samples had high enough density to withstand wear tests, they were not ideal for consideration as a structural material. Further studies are needed to improve densification and overall strength of these low friction composites for structural use.

Applied pressure during PECS shortens the diffusion path between the particles but more importantly it multiplies dislocation density at particle contacts, therefore, densification rate can be improved by high applied pressure [38]. Although in his work the applied sintering temperature was relatively low (<1000 °C) for sintering of ZrO_2, for addressing the second issue, high applied pressure helped in achieving dense compacts owing to the phenomenon above.

4.2. Nano-mechanical and friction of $WO_{2.9}$

In certain tribological conditions hardness and related compressive strength are the most dominant factors that determine the lifetime of a component as e.g. in abrasive wear. However, solid lubrication allows two counter surfaces interact in such a way that one can slide on another avoiding indentation of non-conformal geometry into the flat, despite poor hardness of the solid lubricant additive. Most typically additives with lamellar crystal structures lower friction (and wear of the whole), owing to low bonding strength between atomic layers in their crystal lattice. In oxygen deficient metal oxides, the low friction is the result of mobility of CS planes. Interaction with an indenter can induce this effect and measured hardness can potentially help to understand it.

Hardness of $WO_{2.9}$ was lower than that of WO_3 despite of only a few missing oxygen atoms from the same monoclinic lattice. The lower hardness of $WO_{2.9}$ in comparison to WO_3 is obviously due to easy slip of dislocations on CS planes in $WO_{2.9}$. DellaCort and Deadmore reported first an increase and then a sudden drop in the hardness of rutile as a function of O/Ti-ratio at 25 °C [52], and Gardos [25] explained the change by structural transition from tetragonal to more oxygen-deficient cubic. Although $WO_{2.9}$ is monoclinic, same as WO_3, it is believed to show a similar reduction of hardness behaviour with rutile, owing to missing oxygen planes. In nanoindentation tests the hardness of $WO_{2.9}$ remained independent of load within the standard deviation of the measurements. Additionally, periodical pop-ins during low load indents suggest activation of rapid plastic deformation and deformation in easy shear planes owing to repetitive nature (Fig. 5c) [48]. The observed pop-in behaviour in the load-controlled nanoindentation is known for a long time in different crystalline materials [53,54]. The pop-ins are seemingly localised bursts of plastic deformation activated shear bands, i.e., small magnitude displacements. The dependence of the pop-ins on the indentation rate also points to localised shear [49].

In nano friction tests, when a sharp tip penetrates a surface, plastic deformation occurs and if there is linear movement, ploughing takes place, leading to material transfer and accumulation in the direction of the movement. Although this effect is known to increase CoF the Berkovich tip showed almost the same CoF for all loads even though there was clear deformation and material transfer during scratching. This behaviour might be related to the deformation of low shear strength CS planes and tip geometry. Spherical tip penetrated deeper in the surface at higher normal loads, which increased ploughing causing more material removal. $WO_{2.9}$ showed significant dependence on the ploughing and normal load against both tip geometries. Ploughing CoF was lower for Berkovich tip and hence also the measured CoF.

4.3. Tribology of ZrO_2 + $WO_{2.9}$ composites

Friction and wear in nano scale have different merits compared to macro scale events. In tribology applications, as in any other structural ones, mechanical strength is needed. Limitations on sintering parameters yielded lower structural strength in composites, which ultimately caused breaking of hard particles from the matrix constituting three body abrasion in wear conditions. This type of surface interaction results in higher friction and severe material loss, consequently causing fractures on the surface of the test specimens. Solid lubrication is mostly pressure induced, e.g. where applied load via counter material generates shear in lattice of $WO_{2.9}$ (or as in lamellar solids, breaks Van del Waals bonds between lattice planes). The reduction of CoF at loads of 5 N – 10 N is explained by the activation of CS planes. A lubricious solid film is formed when softer material is smeared onto the wear track ultimately protecting the composite surface from extreme wear.

At a maximum pressure of 1.40 GPa friction was significantly reduced, this trend was also observed at higher contact pressures. The

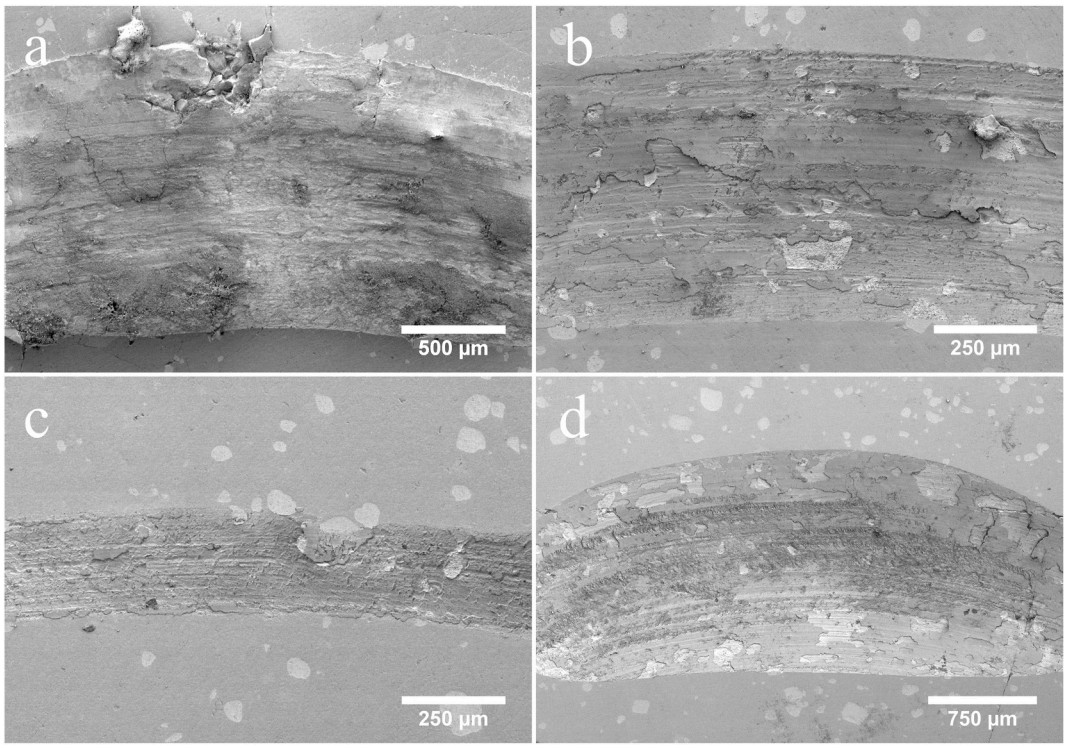

Fig. 10. SEM images of wear tracks from tests with a) 1 N, b) 5 N, c) 10 N and d) 20 N.

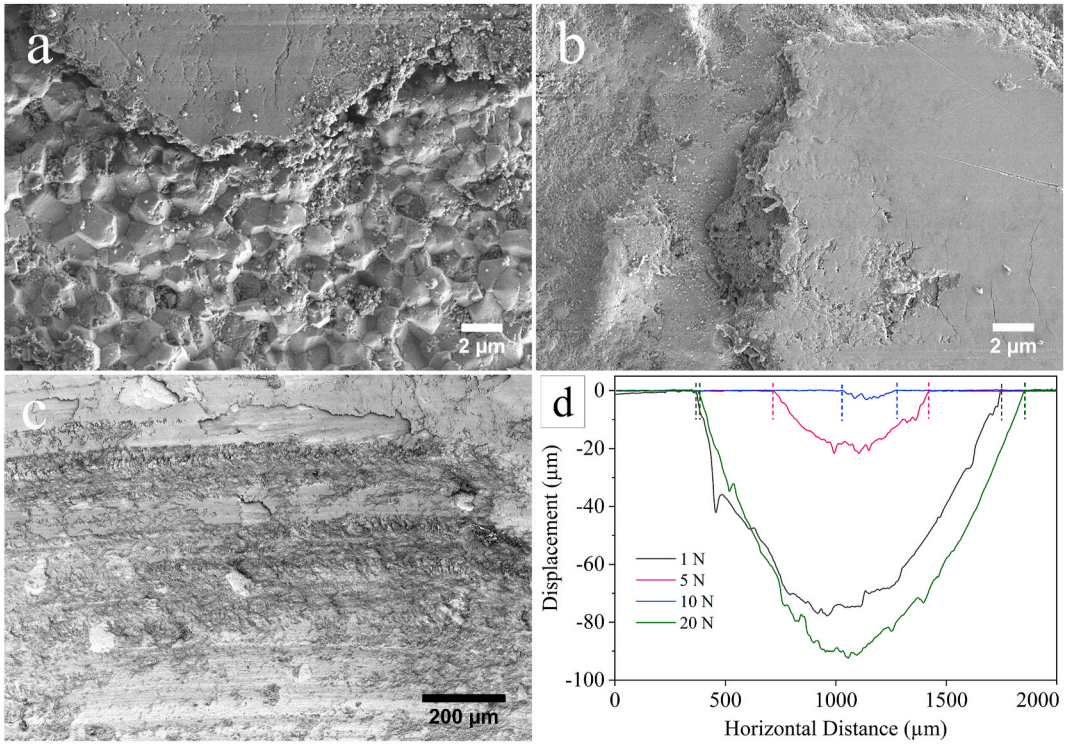

Fig. 11. Difference in wear mechanism in wear tracks from a) 5 N, b) 10 N and c) 20 N tests, and d) wear track profiles for all the applied loads.

compoistes were low friction materials rather than wear resistant ones. The average CoF of n-ZrO_2 + 10 vol% $WO_{2.9}$ against alumina was 0.108 ± 0.030, which is a relatively low value for a bulk ceramic composite. For sake of comparison, hydrogenated or hydrogen free amorphous DLC films in ambient air under 50% humidity have CoF of 0.05 – 0.20 [55], yttria stabilized tetragonal zirconia (YSZ) has CoF of 0.40, and YSZ with 20 wt% Al_2O_3 and 50 wt% MoS_2 or $SrSO_4$ has CoF of 0.10 under the same atmospheric conditions against the same counter material as in this study [56]. In addition to the remarkable friction properties at room temperature, it is believed that the mechanical strength and thus the wear properties of the composite could be improved by optimizing the high-pressure sintering or using a modified matrix.

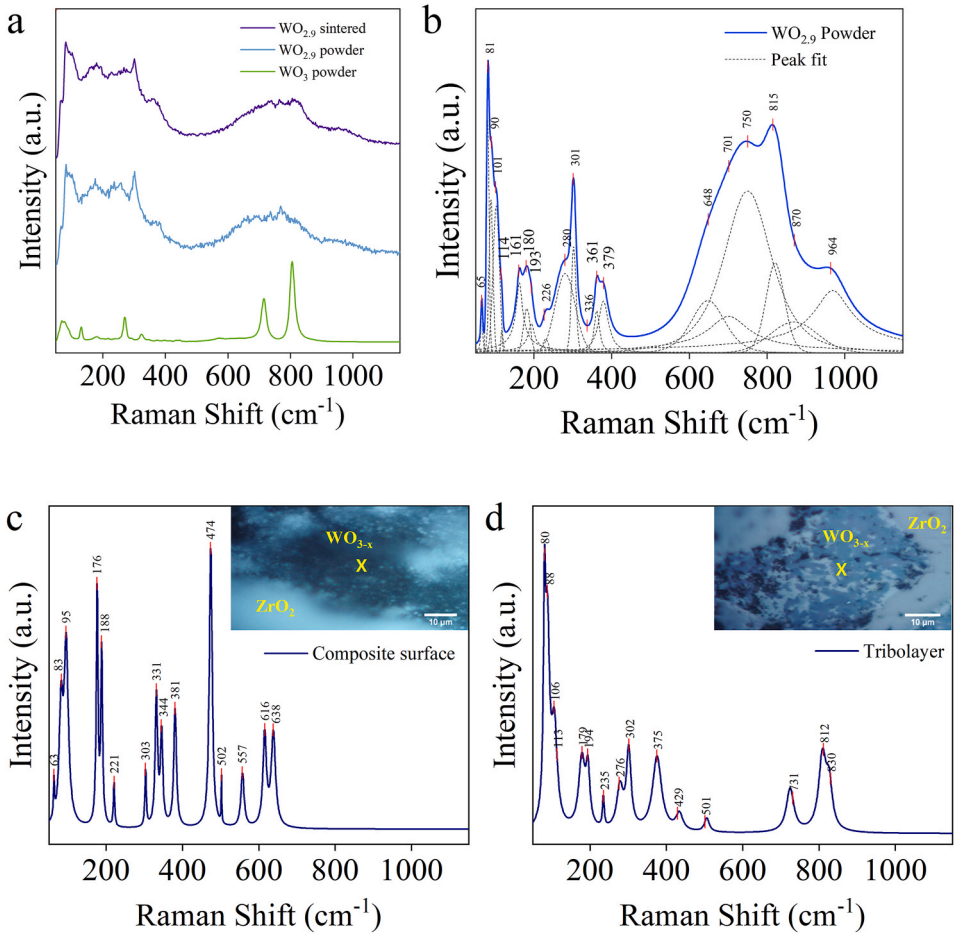

Fig. 12. Raman spectra of (a) WO_3 and $WO_{2.9}$ powders and $WO_{2.9}$ after annealing and sintering, (b) $WO_{2.9}$ powder after fitting, and n-ZrO_2 + 10 vol% $WO_{2.9}$ composite from (c) outside and (d) inside the wear track with optical images in picture and X marking the analysis spot (background removal and peak fitting were applied to b-d).

Low friction properties of the present composites are attributed to the CS oxide within the ceramic matrix, and its presence within the wear track requires some further consideration. The XRD measurements were effective for identifying the phase transformations following vacuum annealing and sintering. Raman spectroscopy is better suited for analysis of the wear track [57]. Details of this method are explained in Ref. [58]. Raman spectroscopy study of the reference material relies on the two earlier publications by other authors [50,51]. In vacuum annealing attempts insufficient reaction temperature or time often yielded to formation of $W_{18}O_{49}$ ($WO_{2.72}$) and/or $W_{17}O_{47}$ ($WO_{2.765}$) phases (unpublished data). The first one was observed by both Chen and Frey in their XRD measurements, and both phases have O/W ratio close to Chen et al.'s electron probe micro analysis (EPMA) results. Vacuum annealing in a sealed container was adopted, whereas in both references the synthesis was made by physical evaporation deposition process, at 840 °C and 1250 °C respectively. In Chen et al.'s work [50] the sub-oxide phase was identified mostly as $W_{18}O_{49}$ in XRD and transmission electron microscopy (TEM) investigations, but based on XPS and EPMA results they concluded the composition to constitute $W_{20}O_{58}$. Similarly, Frey et al. [51] also obtained mixture of several WO_{3-x} phases (e.g. $W_{20}O_{58}$, $W_{18}O_{49}$, WO_2 and W_nO_{3n-1} (n: 4, 5, 6)) under H_2/Ar gas flow for different durations. Reduction under gas flow is a progressive process and although the main reaction is controllable by applied temperature and time, reaction continues below the reaction zone of reducing agent and material surface. For example, if a round WO_3 particle is heated under a reducing gas (e.g. H_2), the reduction reaction will start at the very top surface using H_2 gas as reductant, but underneath the surface, the WO_3 core will react with the newly formed WO_{3-x} (as the reductant), and as a result the reduction reaction will be sustained along the radius. It is possible to contain the outcome of the reaction with a single product when the oxide and the reductant exists only in stochiometric amounts. In our earlier attempts on synthesis of CS oxide we also experimented the reduction under hydrogen flow at 670 °C. This resulted in very fast reaction without any control on the phases in the final mixture (unpublished data). In the present study, XRD measurements were performed on polycrystalline powder, and all the peaks in the spectrum from reference material were identified for monoclinic $WO_{2.9}$. Another complication with Raman measurements (in addition to missing reference spectrum) comes from the apparatus itself. Oxidation by applied laser during Raman spectroscopy is a known phenomenon. High applied laser power or elongated measurements cause instantaneous oxidation and yield to peak shift towards WO_3 positions while $WO_{2.9}$ peaks diminish and eventually disappear in the spectrum, which is well covered e.g. in Ref. [50]. Hence the laser power was kept as low as possible in order to allow acquisition of a reasonable spectrum. Although major characteristic peaks of $W_{20}O_{58}$ were observed in the spectra of the reference material, similar shift for the major bands above 800 cm^{-1} was also observed in this study. In summary, the observed small differences in Raman measurements compared to reference articles are due to differences in synthesis methods and consequently differences in acquired WO_{3-x} phase. Peak shift in XRD measurements and deviation in atomic positions of oxygen atoms based on calculations from XRD data could also explain the shift in Raman bands. In the investigation of the wear tracks the Raman spectrum from inside the

wear track showed less absorption and thus the peak fitting and identification was more effective. In a wear track the tribolayer or wear debris is composed of mixture of materials from counter materials and tribo-products. WO_3 was observed frequently during Raman analysis, but CS oxide phase was clearly present in the tribolayer. Continuity of this layer is dependent on many factors and in this work applied load had significant influence, changing the friction properties accordingly.

5. Conclusions and remarks

Based on the results presented the following conclusions can be made:

I) Magnéli phase oxide $W_{20}O_{58}$ was studied as a solid lubricant within a ceramic matrix. Self-lubricating $ZrO_2 + WO_{2.9}$ composites were synthesized by pulsed electric current sintering. In-situ synthesis of $WO_{2.9}$ phase was achieved when WO_3 which was initially introduced to hard matrix, was reduced during sintering. High pressure sintering was adopted in order to keep the sintering temperature below 1000 °C.

II) Nano-mechanical and friction properties of $W_{20}O_{58}$ CS oxide were studied. As a monolithic material it proved to stand as a good candidate for a solid lubricant with low CoF while having lower hardness than WO_3. Raman spectroscopy studies of $W_{20}O_{58}$ CS oxide compared favourably with previous reports showing only minor variations in structure owing to differences in synthesis methods. Reference CS oxide was synthesized by vacuum annealing in sealed containers in relatively large amounts which was adequate for synthesis of polycrystalline composites.

III) Presence of $WO_{2.9}$ reduced the CoF significantly at room temperature. Applied normal load in testing conditions influenced CoF drastically. ZrO_2 + 10 vol% $WO_{2.9}$ composite had the lowest CoF under 10 N applied load, i.e. 0.108 ± 0.030. The same material had wear rate of 4.82×10^{-11} mm^3/Nm that was an order of a magnitude lower than other test materials. The composites can be regarded as low friction composites rather than wear resistant materials.

Author contributions

M. Erkin Cura: Conceptualization, Methodology, Investigation, Writing - Original Draft, Visualization.

Michal Trebala: Investigation, Data curation.

Yanling Ge: Investigation, Validation.

Piotr Klimczyk: Resources.

Simo-Pekka Hannula: Supervision, Writing - Review & Editing, Funding acquisition.

Declaration of competing interest

The authors declare that they have no known competing financial interests or personal relationships that could have appeared to influence the work reported in this paper.

Acknowledgement

This work was supported partially within the framework of the SINTERCER project (REGPOT-2012-2013-1 EUFP7, project no. 316232) by the European Commission under the FP7 Specific Programme 'Capacities'), and by Academy of Finland via Graduate School for Advanced Materials and Processes (Grant118728). Dr. Ajai Iyer is acknowledged for his help in Raman measurements and Mr. Andreas Friman for his help with tribology tests. Mr. Joonas Lehtonen is acknowledged for helpful discussions.

Appendix A. Supplementary data

Supplementary data to this article can be found online at https://doi.org/10.1016/j.wear.2021.203920.

References

[1] A.A. Voevodin, C. Muratore, S.M. Aouadi, Hard coatings with high temperature adaptive lubrication and contact thermal management: Review, Surf. Coating. Technol. 257 (2014) 247–265, https://doi.org/10.1016/j.surfcoat.2014.04.046.
[2] S. Zhang, T. Ma, A. Erdemir, Q. Li, Tribology of two-dimensional materials: from mechanisms to modulating strategies, Mater. Today 26 (2019) 67–86, https://doi.org/10.1016/j.mattod.2018.12.002.
[3] Y. Liu, X. Ge, J. Li, Graphene lubrication, Appl. Mater. Today 20 (2020) 100662, https://doi.org/10.1016/j.apmt.2020.100662.
[4] X. Chen, J. Li, Superlubricity of carbon nanostructures, Carbon 158 (2020) 1–23, https://doi.org/10.1016/j.carbon.2019.11.077.
[5] J.-H. Ouyang, X.-S. Liang, High-temperature solid lubricating materials, in: Q. J. Wang, Y.-W. Chung (Eds.), Encyclopedia of Tribology, Springer US, Boston, MA, 2013, pp. 1671–1681.
[6] M. Kalin, Influence of flash temperatures on the tribological behaviour in low-speed sliding: a review, Mater. Sci. Eng. 374 (2004) 390–397, https://doi.org/10.1016/j.msea.2004.03.031.
[7] K. Holmberg, A. Matthews, Coatings Tribology: Properties, Mechanisms, Techniques and Applications in Surface Engineering, second ed., Elsevier Science, UK, 2009.
[8] Y. Meng, J. Xu, Z. Jin, B. Prakash, Y. Hu, A review of recent advances in tribology, Friction 8 (2020) 221–300, https://doi.org/10.1007/s40544-020-0367-2.
[9] H.E. Sliney, Solid lubricant materials for high temperatures: a review, Tribol. Int. 15 (1982) 303–315, https://doi.org/10.1016/0301-679X(82)90089-5.
[10] T.W. Scharf, S.V. Prasad, Solid lubricants: a review, J. Mater. Sci. 48 (2013) 511–531, https://doi.org/10.1007/s10853-012-7038-2.
[11] S. Zhu, J. Cheng, Z. Qiao, J. Yang, High temperature solid-lubricating materials: a review, Tribol. Int. 133 (2019) 206–223, https://doi.org/10.1016/j.triboint.2018.12.037.
[12] J.H. Ouyang, S. Sasaki, T. Murakami, K. Umeda, The synergistic effects of CaF_2 and Au lubricants on tribological properties of spark-plasma-sintered $ZrO_2(Y_2O_3)$ matrix composites, Mater. Sci. Eng. 386 (2004) 234–243, https://doi.org/10.1016/j.msea.2004.07.059.
[13] S.M. Aouadi, D.P. Singh, D.S. Stone, K. Polychronopoulou, F. Nahif, C. Rebholz, et al., Adaptive VN/Ag nanocomposite coatings with lubricious behavior from 25 to 1000 °C, Acta Mater. 58 (2010) 5326–5331, https://doi.org/10.1016/j.actamat.2010.06.006.
[14] T.W. Scharf, P.G. Kotula, S.V. Prasad, Friction and wear mechanisms in MoS_2/Sb_2O_3/Au nanocomposite coatings, Acta Mater. 58 (2010) 4100–4109, https://doi.org/10.1016/j.actamat.2010.03.040.
[15] A. Erdemir, A crystal-chemical approach to lubrication by solid oxides, Tribol. Lett. 8 (2000) 97, https://doi.org/10.1023/a:1019183101329.
[16] B. Prakash, J.P. Celis, The lubricity of oxides revised based on a polarisability approach, Tribol. Lett. 27 (2007) 105–112, https://doi.org/10.1007/s11249-007-9223-z.
[17] A.D. Wadsley, Nonstoichiometric metal oxides, in: R. Ward (Ed.), Nonstoichiometric Compounds, American Chemical Society, Washington, D.C., 1963, pp. 23–36.
[18] A. Magnéli, The crystal structures of Mo_9O_{26} (beta'-molybdenum oxide) and Mo_8O_{23} (beta-molybdenum oxide), Acta Chem. Scand. 2 (1948) 501–517, https://doi.org/10.3891/acta.chem.scand.02-0501.
[19] A. Magnéli, The crystal structure of Mo_4O_{11} (gamma-molybdenum oxide), Acta Chem. Scand. 2 (1948) 861–871, https://doi.org/10.3891/acta.chem.scand.02-0861.
[20] A. Magnéli, Structures of the ReO_3-type with recurrent dislocations of atoms: 'Homologous series' of molybdenum and tungsten oxides, Acta Crystallogr. 6 (1953) 495–500, https://doi.org/10.1107/S0365110X53001381.
[21] S. Andersson, B. Collén, U. Kuylenstierna, A. Magnéli, Phase analysis studies on the titanium-oxygen system, Acta Chem. Scand. 11 (1957) 1606–1607, https://doi.org/10.3891/acta.chem.scand.11-1641.
[22] S. Andersson, L. Jahnberg, Crystal structure studies on the homologous series Ti_nO_{2n-1}, V_nO_{2n-1} and $ti_{n-2}Cr_2O_{2n-1}$, Ark. Kemi 21 (1963) 413–426.
[23] M.N. Gardos, The effect of anion vacancies on the tribological properties of rutile (TiO_{2-x}), Tribol. Trans. 31 (1988) 427–436, https://doi.org/10.1080/10402008808981844.
[24] M.N. Gardos, H.S. Hong, W.O. Winer, The effect of anion vacancies on the tribological properties of rutile (TiO_{2-x}), part II: experimental evidence, Tribol. Trans. 33 (1990) 209–220, https://doi.org/10.1080/10402009008981949.
[25] M.N. Gardos, Magnéli phases of anion-deficient rutile as lubricious oxides. Part I. Tribological behavior of single-crystal and polycrystalline rutile (Ti_nO_{2n-1}), Tribol. Lett. 8 (2000) 65–78, https://doi.org/10.1023/a:1019122915441.
[26] M.N. Gardos, Magnéli phases of anion-deficient rutile as lubricious oxides. Part II. Tribological behavior of Cu-doped polycrystalline rutile (Ti_nO_{2n-1}), Tribol. Lett. 8 (2000) 79–96, https://doi.org/10.1023/A:1019174932279.
[27] M. Woydt, A. Skopp, I. Dörfel, K. Witke, Wear engineering oxides/anti-wear oxides, Wear 218 (1998) 84–95, https://doi.org/10.1016/S0043-1648(98)00181-1.
[28] M. Woydt, Tribological characteristics of polycrystalline Magnéli-type titanium dioxides, Tribol. Lett. 8 (2000) 117–130, https://doi.org/10.1023/A:1019170831371.
[29] O. Storz, H. Gasthuber, M. Woydt, Tribological properties of thermal-sprayed Magnéli-type coatings with different stoichiometries (Ti_nO_{2n-1}), Surf. Coating. Technol. 140 (2001) 76–81, https://doi.org/10.1016/S0257-8972(01)01024-6.
[30] M. Woydt, Sub-stoichiometric oxides for wear resistance, Wear 440–441 (2019), https://doi.org/10.1016/j.wear.2019.203104, 203104.

[31] G. Gassner, P.H. Mayrhofer, K. Kutschej, C. Mitterer, M. Kathrein, A new low friction concept for high temperatures: lubricious oxide formation on sputtered VN coatings, Tribol. Lett. 17 (2004) 751–756, https://doi.org/10.1007/s11249-004-8083-z.
[32] N. Fateh, G. Fontalvo, G. Gassner, C. Mitterer, The beneficial effect of high-temperature oxidation on the tribological behaviour of V and VN coatings, Tribol. Lett. 28 (2007) 1–7, https://doi.org/10.1007/s11249-007-9241-x.
[33] R. Franz, C. Mitterer, Vanadium containing self-adaptive low-friction hard coatings for high-temperature applications: a review, Surf. Coating. Technol. 228 (2013) 1–13, https://doi.org/10.1016/j.surfcoat.2013.04.034.
[34] G. Gassner, P.H. Mayrhofer, K. Kutschej, C. Mitterer, M. Kathrein, Magnéli phase formation of PVD Mo-N and W-N coatings, Surf. Coating. Technol. 201 (2006) 3335–3341, https://doi.org/10.1016/j.surfcoat.2006.07.067.
[35] M.E. Cura, X.W. Liu, U. Kanerva, S. Varjus, A. Kivioja, O. Söderberg, et al., Friction behavior of alumina/molybdenum composites and formation of MoO_{3-x} phase at 400 °C, Tribol. Int. 87 (2015) 23–31, https://doi.org/10.1016/j.triboint.2015.02.010.
[36] E. Lugscheider, O. Knotek, K. Bobzin, S. Bärwulf, Tribological properties, phase generation and high temperature phase stability of tungsten- and vanadium-oxides deposited by reactive MSIP-PVD process for innovative lubrication applications, Surf. Coating. Technol. 133–134 (2000) 362–368, https://doi.org/10.1016/S0257-8972(00)00963-4.
[37] T. Polcar, N.M.G. Parreira, A. Cavaleiro, Tungsten oxide with different oxygen contents: sliding properties, Vacuum 81 (2007) 1426–1429, https://doi.org/10.1016/j.vacuum.2007.04.001.
[38] G. Lee, C. Manière, J. McKittrick, E.A. Olevsky, Electric current effects in spark plasma sintering: from the evidence of physical phenomenon to constitutive equation formulation, Scripta Mater. 170 (2019) 90–94, https://doi.org/10.1016/j.scriptamat.2019.05.040.
[39] J. Booth, T. Ekström, E. Iguchi, R.J.D. Tilley, Notes on phases occurring in the binary tungsten-oxygen system, J. Solid State Chem. 41 (1982) 293–307, https://doi.org/10.1016/0022-4596(82)90149-9.
[40] A. Magnéli, Crystal structure studies on beta-tungsten oxide, Ark. Kemi 1 (1949) 513–523.
[41] H.A. Wriedt, The O-W (Oxygen-tungsten) System. Phase Equilibria Diagrams Online Database (NIST Standard Reference Database 31). 1989/08/01, The American Ceramic Society and the National Institute of Standards and Technology, 2020.
[42] L.L.Y. Chang, M.G. Scroger, B. Phillips, Condensed Phase Relations in the Systems ZrO2-WO2-WO3 and HfO2-WO2-WO3. Phase Equilibria Diagrams Online Database (NIST Standard Reference Database 31), The American Ceramic Society and the National Institute of Standards and Technology, 2020.
[43] U. Anselmi-Tamburini, J.E. Garay, Z.A. Munir, A. Tacca, F. Maglia, G. Chiodelli, et al., Spark plasma sintering and characterization of bulk nanostructured fully stabilized zirconia: Part II. Characterization studies, J. Mater. Res. 19 (2004) 3263–3269, https://doi.org/10.1557/JMR.2004.0424.
[44] O. Guillon, J. Gonzalez-Julian, B. Dargatz, T. Kessel, G. Schierning, J. Räthel, et al., Field-assisted sintering technology/spark plasma sintering: mechanisms, materials, and technology developments, Adv. Eng. Mater. 16 (2014) 830–849, https://doi.org/10.1002/adem.201300409.
[45] J.E. Alaniz, F.G. Perez-Gutierrez, G. Aguilar, J.E. Garay, Optical properties of transparent nanocrystalline yttria stabilized zirconia, Opt. Mater. 32 (2009) 62–68, https://doi.org/10.1016/j.optmat.2009.06.004.
[46] M.A.A. Attia, S. Garroni, D. Chiriu, C. Ricci, F. Delogu, R. Orrù, et al., X-ray induced color change on dense yttria samples obtained by spark plasma sintering, Chem. Phys. Lett. 618 (2015) 108–113, https://doi.org/10.1016/j.cplett.2014.11.009.
[47] J.L. Enriquez-Carrejo, M.A. Ramos, J. Mireles-Jr-Garcia, A. Hurtado-Macias, Nano-mechanical and structural study of WO_3 thin films, Thin Solid Films 606 (2016) 148–154, https://doi.org/10.1016/j.tsf.2016.03.054.
[48] C.A. Schuh, Nanoindentation studies of materials, Mater. Today 9 (2006) 32–40, https://doi.org/10.1016/S1369-7021(06)71495-X.
[49] C.A. Schuh, T.G. Nieh, Y. Kawamura, Rate dependence of serrated flow during nanoindentation of a bulk metallic glass, J. Mater. Res. 17 (2002) 1651–1654, https://doi.org/10.1557/JMR.2002.0243.
[50] J. Chen, D. Lu, W. Zhang, F. Xie, J. Zhou, L. Gong, et al., Synthesis and Raman spectroscopic study of $W_{20}O_{58}$ nanowires, J. Phys. D Appl. Phys. 41 (2008) 115305, https://doi.org/10.1088/0022-3727/41/11/115305.
[51] G.L. Frey, A. Rothschild, J. Sloan, R. Rosentsveig, R. Popovitz-Biro, R. Tenne, Investigations of nonstoichiometric tungsten oxide nanoparticles, J. Solid State Chem. 162 (2001) 300–314, https://doi.org/10.1006/jssc.2001.9319.
[52] C. DellaCorte, D.L. Deadmore, Vickers Indentation Hardness of Stoichiometric and Reduced Single Crystal TiO_2 (Rutile) from 25 to 800 °C. Technical Memorandum - 105959, NASA, Ohio, US, 1993.
[53] T.F. Page, W.C. Oliver, C.J. McHargue, The deformation behavior of ceramic crystals subjected to very low load (nano)indentations, J. Mater. Res. 7 (1992) 450–473, https://doi.org/10.1557/JMR.1992.0450.
[54] S.G. Corcoran, R.J. Colton, E.T. Lilleodden, W.W. Gerberich, Anomalous plastic deformation at surfaces: nanoindentation of gold single crystals, Phys. Rev. B 55 (1997) R16057–R16060, https://doi.org/10.1103/PhysRevB.55.R16057.
[55] H. Ronkainen, K. Holmberg, Environmental and thermal effects on the tribological performance of DLC coatings, in: C. Donnet, A. Erdemir (Eds.), Tribology of Diamond-Like Carbon Films: Fundamentals and Applications, Springer US, Boston, MA, 2008, pp. 155–200.
[56] J.H. Ouyang, Y.F. Li, Y.M. Wang, Y. Zhou, T. Murakami, S. Sasaki, Microstructure and tribological properties of $ZrO_2(Y_2O_3)$ matrix composites doped with different solid lubricants from room temperature to 800 °C, Wear 267 (2009) 1353–1360, https://doi.org/10.1016/j.wear.2008.11.017.
[57] K. Zhang, Z. Xu, A. Rosenkranz, Y. Song, T. Xue, F. Fang, Surface- and tip-enhanced Raman scattering in tribology and lubricant detection - a prospective, Lubricants 7 (2019) 81, https://doi.org/10.3390/lubricants7090081.
[58] R.R. Jones, D.C. Hooper, L. Zhang, D. Wolverson, V.K. Valev, Raman techniques: fundamentals and frontiers, Nanoscale Res. Lett. 14 (2019) 231, https://doi.org/10.1186/s11671-019-3039-2.
[59] M. Varenik, S. Cohen, E. Wachtel, A. Frenkel, et al., Oxygen vacancy ordering and viscoelastic mechanical properties of doped ceria ceramics, Scripta Mater. 163 (2019) 19–23, https://doi.org/10.1016/j.scriptamat.2018.12.024, 1359-6462.